

Accepted by the ApJS on April 11, 2016

## A STATISTICAL STUDY OF THE AVERAGE IRON CHARGE STATE DISTRIBUTIONS INSIDE MAGNETIC CLOUDS FOR SOLAR CYCLE 23

H.Q. SONG<sup>1</sup>, Z. ZHONG<sup>1</sup>, Y. CHEN<sup>1</sup>, J. ZHANG<sup>2</sup>, X. CHENG<sup>3</sup>, L. Zhao<sup>4</sup>, Q. HU<sup>5</sup>, AND G. LI<sup>5</sup>

*1 Shandong Provincial Key Laboratory of Optical Astronomy and Solar-Terrestrial Environment, and Institute of Space Sciences, Shandong University, Weihai, Shandong 264209, China*

`hqsong@sdu.edu.cn`

*2 School of Physics, Astronomy and Computational Sciences, George Mason University, Fairfax, VA 22030, USA*

*3 School of Astronomy and Space Science, Nanjing University, Nanjing, Jiangsu 210093, China*

*4 Department of Atmospheric, Oceanic, and Space Sciences, University of Michigan, Ann Arbor, MI 48105, USA*

*5 Department of Space Science and CSPAR, University of Alabama in Huntsville, Huntsville, AL 35899, USA*

### ABSTRACT

Magnetic clouds (MCs) are the interplanetary counterpart of coronal magnetic flux ropes. They can provide valuable information to reveal the flux rope characteristics at their eruption stage in the corona, which are unable to be explored in situ at present. In this paper, we make a comprehensive survey of the average iron charge state ( $\langle Q \rangle_{\text{Fe}}$ ) distributions inside 96 MCs for solar cycle 23 using *ACE* (*Advanced Composition Explorer*) data. As the  $\langle Q \rangle_{\text{Fe}}$  in the solar wind are typically around 9+ to 11+, the Fe charge state is defined as high when the  $\langle Q \rangle_{\text{Fe}}$  is larger than 12+, which implies the existence of a considerable amount of Fe ions with high charge states (e.g.,  $\geq 16+$ ). The statistical results show that the  $\langle Q \rangle_{\text{Fe}}$  distributions of 92 ( $\sim 96\%$ ) MCs can be classified into four groups with different characteristics. In group A (11 MCs), the  $\langle Q \rangle_{\text{Fe}}$  shows a bimodal distribution with both peaks higher than 12+. Group B (4 MCs) presents a unimodal distribution of  $\langle Q \rangle_{\text{Fe}}$  with its peak higher than 12+. In groups C (29 MCs) and D (48 MCs), the  $\langle Q \rangle_{\text{Fe}}$  remains higher and lower than 12+ throughout *ACE* passage through the MC, respectively. Possible explanations to these distributions are discussed.

*Subject headings:* Sun: coronal mass ejections (CMEs) – magnetic reconnection – Sun: flares

## 1. INTRODUCTION

Coronal mass ejections (CMEs) are the most energetic eruption in the solar system. After CMEs propagate into interplanetary space, they are called interplanetary coronal mass ejections (ICMEs), which can cause geomagnetic activities and affect the satellites, power grids and GPS navigation systems when they interact with the geo-magnetosphere (Gosling et al. 1991; Zhang et al. 2003; Zhang et al. 2007). ICMEs are extensively investigated by solar/space physics community (Gopalswamy 2006; Jian et al. 2006; Kilpua et al. 2013; Chi et al. 2015) for their important role in space weather studies. Magnetic clouds (MCs, Burlaga et al. 1981), large interplanetary magnetic flux rope structures embedded in ICMEs, are more attractive as they usually cause stronger geomagnetic storms compared to those ICMEs without MCs (Wu & Lepping 2011, 2015; Lepping et al. 2011, 2015), and also because they have relatively regular magnetic structures and can be fitted with flux rope reconstruction methods (Lepping et al. 1990; Hu & Sonnerup 2002; Wang et al. 2015).

By investigating the properties of MCs with in situ observations, one can reveal the flux rope formation and eruption processes in the corona. However, most MC parameters, e.g., the density, temperature, velocity, volume and morphology, as well as magnetic field strength, will experience large variation during the propagation from near the Sun to 1 AU due to their expansion, acceleration/deceleration, and interaction with other interplanetary structures. This complicates efforts to investigate the flux rope formation and eruption in the corona through in situ data.

Fortunately, the charge states of ions inside MCs are frozen before the flux ropes leave the corona (e.g., Rakowski et al. 2007; Ko et al. 2010; Lynch et al. 2011; Gruesbeck et al. 2011; Lepri et al. 2012) and therefore may reflect their evolution history near the Sun. Usually, the appearance of high ionic charge states implies high electron temperature and is attributed to magnetic reconnection occurring along the current sheet connecting the flux rope to flare loops (Bemporad et al. 2006; Ko et al. 2013; Song et al. 2015b). As reconnection continues toward higher altitude, the flux rope will be added with more layers consisting of reconnected magnetic field lines. And the heated plasma will correspondingly fill in the flux rope structure along these field lines giving rise to an onion-layer morphology (Ko et al. 2013). Therefore, high ionic charge states inside MCs may provide direct signatures of reconnection in the post-CME current sheet, which is very helpful to address some important unresolved issues of CMEs.

One heated debate associated with CME is that whether the flux ropes exist prior to the eruption or they are formed during the eruption (Song et al. 2014a, and references therein). Some numerical simulations (Chen 1996; Lin & Forbes 2000) and observations (Zhang et al. 2012; Patsourakos et al. 2013; Cheng et al. 2013, 2014; Song et al. 2014b, 2015b) support that flux ropes can exist prior to the eruption, while other simulations (Mikić & Linker 1994) and observations (Song et al. 2014a; Ouyang et al. 2015) demonstrate that flux ropes can also be formed during the eruption. When the eruption involves a pre-existing flux rope with relatively low temperature, which is surrounded by heated plasmas formed through magnetic reconnection in the current sheet,

we would expect to detect an MC with low-ionization-state center and high-ionization-state shell (Lin et al. 2004; Ko et al. 2013; Song et al. 2015b). On the contrary, when the flux rope is mostly formed during the eruption, a more ionized center might be observed due to stronger heating and higher densities at lower heights (Ko et al. 2013). It has been reported that the  $[\text{Fe}_{XVIII}]$  line intensity in the post-CME current sheet decreases with height, supporting this suggestion (Ciaravella et al. 2013).

Iron is an astrophysically abundant heavy element. Its heavy mass allows the iron ions, detected in situ, to be well separated from other abundant heavy ions in the normal solar wind and ICMEs due to significantly less interference from other species. This is because ions are distinguished based on their mass and charge (mass/charge) by present instruments (Gloeckler et al. 1998; von Steiger et al. 2000). It has been suggested that Fe ions are more affected by the continuing heating along a more extended space of the plasma flow near the Sun, and other species such as C and O ions are mainly sensitive to the heating processes at the earlier stage (e.g., Ko et al. 2010; Gruesbeck et al. 2011; Lepri et al. 2012). Therefore, the in situ charge states of different ion species can not be compared with each other in a straightforward manner. Here we focus our study on Fe ions. Average Fe charge states ( $\langle Q \rangle_{\text{Fe}}$ ) in the solar wind are typically around 9+ to 11+ (e.g., Lepri et al. 2001). Based on the comparisons of charge state distributions between the normal solar wind and ICMEs with high Fe charge states, Lepri & Zurbuchen (2004) determined a reasonable threshold of  $\langle Q \rangle_{\text{Fe}}$  as 12+, above which it implies a considerable amount of high Fe charge states in ICMEs and vice versa. High Fe charge states above this threshold have been observed in over 50% ICMEs, therefore it has been used as one complementary identifier of ICMEs (Lepri et al. 2001; Lepri & Zurbuchen 2004). However, a comprehensive analysis of  $\langle Q \rangle_{\text{Fe}}$  distribution inside MCs remains absent.

In this paper, we make a comprehensive survey of  $\langle Q \rangle_{\text{Fe}}$  distributions of 96 MCs for solar cycle 23 using ACE data and  $\sim 96\%$  of them (92 MCs) can be classified into four groups, shedding more light on the flux rope formation process. The instruments are introduced in Section 2, and the data analysis is presented in Section 3. Section 4 discusses possible explanations to the results, which is followed by a summary in Section 5.

## 2. INSTRUMENTS

The Fe charge state is obtained using the Solar Wind Ion Composition Spectrometer (SWICS, Gloeckler et al. 1998) on board the *Advanced Composition Explorer (ACE)* that launched in 1997 and orbits around the L1 point. As a mass spectrometer, SWICS consists of a time-of-flight (TOF) system and an energy resolving solid-state detector (SSD). The TOF system measures the speed of each ion and the SSD determines its residual energy, which allow the determination of mass, charge, and energy of the detected ion. SWICS can determine the density, bulk speed, and the thermal speed of almost 40 heavy ions and provide the charge state distributions and abundances of  $\sim 10$  elements (also see Lepri et al. 2001). In this study, we use the newly released SWICS 1.1

level 2 data, which are calculated by an improved calibration algorithm and have better accuracy from the previous versions (Shearer et al. 2014). The process for removing accidental coincidence events has been improved, leading to an increase in identification of rare ions such as  $\text{Fe}^{6+}$  and  $\text{Fe}^{7+}$ . Except the ionic charge state, we also use the data from MAG (Smith et al. 1998) and SWEFAM (McComas et al. 1998) on board *ACE* for the magnetic field and plasma measurements of associated MCs.

### 3. DATA ANALYSIS

MCs in the solar wind can be identified if the magnetic field strength is higher than the surrounding background, the field direction rotates smoothly through a large angle, and the proton temperature is lower compared to the environment (Burlaga et al. 1981). In this study, we choose to use the MC lists published by other authors, instead of examining MCs by ourselves. This separates issues related to the MC identification and to the ionic charge state analysis, making our study more focused. As no unique and fully objective way has been developed to identify MCs in interplanetary space (e.g., Huttunen et al. 2005), some subjective judgements may influence the decision on whether a candidate is an MC or not, as well as exact locations of its front and back boundaries. Therefore, some disagreements on MC boundary locations often exist among different MC lists. We will discuss how this may affect our statistical results in Section 4.

#### 3.1. MC Lists

The public 1-h resolution  $\langle Q \rangle \text{Fe}$  data from SWICS are available on the website of the *ACE* science center since February 1998 (<http://www.srl.caltech.edu/ACE/ASC/index.html>), so we include the MCs detected at L1 between February 1998 and December 2009 in this survey. Two MC lists are used here, one is published by Huttunen et al. (2005) that included 2 MCs analyzed with *WIND* data in February 1998 at L1 point and 60 MCs analyzed with *ACE* data from March 1998 to December 2003 (See Table 2 of their paper). The other one is from *WIND* MFI team, which provided MCs from February 1995 to December 2009 ([http://wind.nasa.gov/mfi/mag\\_cloud\\_S1.html](http://wind.nasa.gov/mfi/mag_cloud_S1.html); Lepping & Wu 2010), including 38 MCs from 2004 to 2009 observed at L1 point. Note *WIND* spacecraft didn't always orbit around L1 from 1994 to 2003, so we didn't use its MC information between 1998 and 2003. Totally, with the above two lists we acquired 100 MCs from February 1998 to December 2009 at L1 point. Among them, 96 MCs have complete Fe charge-state data as recorded by SWICS, and 2/2 MCs have incomplete/no Fe charge-state data. The typical scale of MC structures is around 0.25 AU (e.g., Lepping et al. 2006),  $\sim 5900$  Earth radii ( $R_E$ ), and the average duration of MCs is close to 20 h (Wu & Lepping, 2011, 2015). When both *WIND* and *ACE* are around L1 point, their separation distance is mostly along the radial direction and generally less than  $240 R_E$ , so except for a time delay of several tens of minutes, their plasma and magnetic field measurements are almost identical. In some cases, there is a lateral separation of about 200

$R_E$  along the east-west direction, which is still significantly smaller than the typical size of the MC near 1 AU, and not considerable. We compared the *WIND* and *ACE* measurements for each MC from 2004 to 2009 and confirmed this point. Therefore, the magnetic field measurement by *WIND* and the charge-state measurement by *ACE* can be used together for the purpose of our study.

### 3.2. Criteria and Statistical Results

Following Lepri & Zurbuchen (2004), the  $\langle Q \rangle_{Fe}$  higher/lower than 12+ is defined as high/normal charge state. With this threshold, we found that there are 50 MCs that contain high charge state and 48 MCs not. This is consistent with the ICME percentage associated with high Fe charge state as reported by Lepri et al. (2001) and Lepri & Zurbuchen (2004). In Figure 1, the histograms display the yearly total number of MCs. The blue/red portions of the bars correspond to MCs without/with high charge state. The line connected by black filled circles shows the yearly sunspot number. Figure 1 shows that the high Fe charge-state MCs present in the rising (1998-1999), maximum (2000), and declining (2001-2005) phases of solar cycle 23, and almost no high Fe charge-state MCs are observed in the past solar minimum (2006-2009).

After inspecting the  $\langle Q \rangle_{Fe}$  distributions inside the 96 MCs with complete Fe charge-state data from SWICS, we find that  $\sim 96\%$  of them (92 MCs) can be divided into 4 groups (A, B, C, and D) based on their distribution characteristics. The rest 4 MCs are included in Group E, which will be discussed later. Table 1 lists the MC durations in every group according to their time sequence. A summary of the classification results is presented in the pie diagram of Figure 2.

To illustrate the  $\langle Q \rangle_{Fe}$  distribution characteristics inside MCs for Groups A – D, we select one representative event from each group, and plot their corresponding observations of the magnetic field, plasma, and Fe charge state in Figures 3-6. Panel (a) presents the total magnetic field strength (black line) and the three components, which are plotted in the Geocentric Solar Ecliptic coordinate. The red, green, and blue lines correspond to the X, Y, and Z components, respectively. The solar wind speed, density, and temperature are presented in panels (b)-(d) sequentially. Panel (e) is the Fe charge state distribution, and the last panel is the  $\langle Q \rangle_{Fe}$  in which the horizontal purple dotted line marks the level of 12+. The locations of the ICME shock (if exists) and MC boundaries are depicted with purple vertical solid line and dot-dashed lines, respectively.

In Group A (11 MCs), the  $\langle Q \rangle_{Fe}$  inside MCs presents a bimodal distribution with its two peaks higher than 12+, and less than 12+ between the peaks as shown in Figure 3(f). It is obvious that a considerable amount of high Fe charge states ( $\sim 16+$ ) appear in this event (Figure 3(e)) resulting in the elevated  $\langle Q \rangle_{Fe}$ . Group B (4 MCs) is defined when the  $\langle Q \rangle_{Fe}$  inside MCs shows a unimodal distribution with its peak higher than 12+ as shown in Figure 4(f). Note the  $\langle Q \rangle_{Fe}$  on either side of the peak is lower than 12+. In Group C (29 MCs), the  $\langle Q \rangle_{Fe}$  remains higher than 12+ during *ACE* passage through the MC as shown in Figure 5(f). Figure 5(e) shows that this event is always associated with lots of Fe charge states as high as  $\geq 16+$ , and the enhancement

Table 1: Classification groups (G) and their MCs at L1 point for solar cycle 23.

G	MC start – end time (UT) yy/mm/dd – mm/dd hh:mm		
A	98/10/19 04:00 – 10/20 06:00	99/04/16 20:00 – 04/17 18:00	99/04/21 12:00 – 04/22 13:00
	00/08/12 05:00 – 08/13 02:00	00/11/06 22:00 – 11/07 15:00	01/03/19 22:00 – 03/21 23:00
	01/05/28 11:00 – 05/29 06:00	01/11/24 17:00 – 11/25 13:00	02/04/17 24:00 – 04/19 01:00
	03/08/18 06:00 – 08/19 11:00	04/11/09 20:54 – 11/10 03:24	
B	01/03/04 16:00 – 03/05 02:00	03/03/20 13:00 – 03/20 22:00	04/08/29 18:42 – 08/30 20:48
	05/12/31 14:48 – 01/01 10:48		
C	98/06/24 12:00 – 06/25 16:00 <sup>a</sup>	98/09/25 08:00 – 09/26 12:00 <sup>a</sup>	99/02/18 14:00 – 02/19 11:00
	00/02/12 12:00 – 02/12 24:00	00/02/21 14:00 – 02/22 12:00 <sup>a</sup>	00/07/11 23:00 – 07/13 02:00
	00/07/15 05:00 – 07/15 14:00	00/07/15 19:00 – 07/16 12:00	00/09/17 23:00 – 09/18 14:00
	00/10/13 17:00 – 10/14 13:00	01/03/27 22:00 – 03/28 05:00	01/04/12 10:00 – 04/13 06:00
	01/04/28 24:00 – 04/29 13:00	01/10/03 01:00 – 10/03 16:00	02/02/28 18:00 – 03/01 10:00
	02/03/19 22:00 – 03/20 10:00 <sup>a</sup>	02/03/24 10:00 – 03/25 12:00 <sup>a</sup>	02/04/20 13:00 – 04/21 15:00 <sup>a</sup>
	03/10/29 12:00 – 10/30 01:00 <sup>a</sup>	03/11/20 11:00 – 11/21 01:00	04/04/04 02:48 – 04/05 14:48
	04/07/22 15:24 – 07/22 23:06 <sup>a</sup>	04/07/24 12:48 – 07/25 13:18	04/11/08 03:24 – 11/08 16:36 <sup>a</sup>
	04/11/10 03:24 – 11/10 11:06	05/05/15 05:42 – 05/15 22:18	05/05/20 07:18 – 05/21 05:18 <sup>a</sup>
	05/06/12 15:42 – 06/13 07:06 <sup>a</sup>	06/12/14 22:48 – 12/15 19:48	
D	98/02/04 05:00 – 02/05 14:00	98/02/17 10:00 – 02/18 04:00	98/03/04 15:00 – 03/05 21:00
	98/06/02 10:00 – 06/02 16:00	98/08/20 08:00 – 08/21 18:00 <sup>b</sup>	98/11/13 04:00 – 11/14 06:00
	99/03/25 16:00 – 03/25 23:00	99/08/09 10:00 – 08/10 14:00	99/08/22 12:00 – 08/23 06:00
	99/09/21 20:00 – 09/22 11:00	99/11/14 01:00 – 11/14 09:00	00/07/13 15:00 – 07/13 24:00
	00/07/31 22:00 – 08/01 12:00	00/08/10 20:00 – 08/11 08:00	00/10/03 15:00 – 10/04 14:00 <sup>b</sup>
	01/04/21 23:00 – 04/22 24:00	01/06/18 23:00 – 06/19 14:00	01/07/10 17:00 – 07/11 23:00
	01/10/31 22:00 – 11/01 18:00	02/05/19 04:00 – 05/19 22:00	02/08/02 06:00 – 08/02 22:00
	02/09/30 23:00 – 10/01 15:00	03/01/27 01:00 – 01/27 15:00 <sup>b</sup>	05/07/17 15:18 – 07/18 03:48
	05/10/31 02:54 – 10/31 20:24	06/02/05 19:06 – 02/06 13:06	06/04/13 14:48 – 04/13 20:48 <sup>b</sup>
	06/04/13 20:36 – 04/14 09:54	06/08/30 21:06 – 08/31 14:54	06/09/30 08:36 – 09/30 21:36
	07/01/14 14:06 – 01/15 06:54	07/03/24 03:06 – 03/24 16:54	07/05/21 22:54 – 05/22 13:36
	07/11/19 23:24 – 11/20 12:54	07/12/25 15:42 – 12/26 06:48	08/12/17 03:06 – 12/17 14:24
	09/01/02 06:06 – 01/02 15:06 <sup>b</sup>	09/02/04 00:06 – 02/04 10:54	09/03/12 00:42 – 03/13 00:42
	09/06/27 15:18 – 06/28 18:18	09/07/21 03:54 – 07/21 17:06	09/09/10 10:24 – 09/10 16:24
	09/09/30 07:54 – 09/30 16:54	09/10/12 12:06 – 10/12 16:48	09/10/17 22:06 – 10/18 07:24
	09/10/29 05:12 – 10/29 22:48	09/11/01 08:48 – 11/02 07:48	09/12/12 19:48 – 12/14 05:18
E	98/05/02 12:00 – 05/03 17:00	98/11/08 23:00 – 11/10 01:00	00/10/28 24:00 – 10/29 23:00
	05/06/15 05:48 – 06/16 07:48		

<sup>a</sup>With one or a few data points lower than 12+.

<sup>b</sup>With one or a few data points higher than 12+.

of high Fe charge states is almost coincident with the passage of the MC. Note the MC  $\langle Q \rangle_{\text{Fe}}$  in Group C can have a broad variation (e.g., 13+~16+) with different patterns. In this study, we do not distinguish these pattern details and classify them into one single group, since we are mainly interested in the appearance of a considerable amount of Fe ions with high charge states, which is defined when the  $\langle Q \rangle_{\text{Fe}}$  is over 12+ (Lepri et al. 2001), and higher  $\langle Q \rangle_{\text{Fe}}$  values simply indicating high charge state Fe ions are more abundant. Group D (48 MCs) includes MCs not associated with high charge states, i.e., with  $\langle Q \rangle_{\text{Fe}}$  less than 12+, as presented in Figure 6. Again, the MC  $\langle Q \rangle_{\text{Fe}}$  in Group D may have some variation as well (e.g., 9+~11+), yet not of interest here.

Panels (e) in Figures 3-6 clearly show that when the  $\langle Q \rangle_{\text{Fe}}$  is larger than 12+, a considerable amount of ions with charge states even higher than 16+ are frequently present. Accordingly, we find that the variation trend of  $\langle Q \rangle_{\text{Fe}}$  is in general consistent with that of the  $\text{Fe}^{\geq 16+}$  abundance (i.e.,  $\text{Fe}^{\geq 16+}/\text{Fe}_{\text{total}}$ , not included here), which is often used as a measure of the unusually enhanced charge states (e.g., Lepri et al. 2001). This supports that the prescribed threshold of 12+ is an appropriate criterion to represent the presence of a considerable amount of high Fe charge states, which can be further verified by checking the complete Fe charge state distributions and  $\langle Q \rangle_{\text{Fe}}$  variations (cyan) within all MCs in Groups A-D as shown in Figure 7. The horizontal white dotted line in each panel marks the level of 12+ for  $\langle Q \rangle_{\text{Fe}}$ . Note only the MC part of the data is plotted with the left/right boundary of each panel being the MC start/end time. It is seen that the Fe charge state distributions present an obvious bi-modal distribution, mainly concentrating around 16+ and/or 10+. In Groups A and B, their distributions appear around 16+ and 10+ at different intervals, with undulating variation fluctuating with the  $\langle Q \rangle_{\text{Fe}}$  trend. Note that if just one or a few discrete  $\langle Q \rangle_{\text{Fe}}$  data points are lower/higher than 12+, i.e., their surroundings are higher/lower than 12+, the discrete ones will be disregarded. In Group C/D, most of the distributions are mainly characterized by charge-state concentration around 16+/10+, consistent with their  $\langle Q \rangle_{\text{Fe}}$  keeping higher/lower than 12+. This confirms that the 12+ condition is indeed an efficient identifier to separate the MC events with high or normal Fe charge state (Lepri & Zurbuchen, 2004). It is of some importance for relevant studies as the SWICS on board *ACE* suffered a hardware anomaly in 2011 and only  $\langle Q \rangle_{\text{Fe}}$  data are available since then. Note one or a few discrete data points in Group C/D are below/beyond 12+ (see notes in Table 1 and corresponding panels in Figure 7), which are disregarded as mentioned above. Two events (20020420 and 20050520) in Group C have 5 continuous data points (less than 22% of their total data points) lower than 12+ near one boundary, while they do not change the  $\langle Q \rangle_{\text{Fe}}$  distribution characteristics obviously and are also neglected.

As mentioned, most MCs (~96%) can be divided into Groups A – D. Four events can not be classified into these groups and are included in Group E. We will discuss possible explanations for all groups in next section.

#### 4. DISCUSSION

In general, ICMEs can either exhibit high Fe charge states or not. Lynch et al. (2011) derived the ionic charge state composition distribution using axisymmetric MHD simulations of CMEs initiated via either flux-cancellation or magnetic breakout mechanism. They concluded that enhanced heavy ionic charge states within the flux rope are a direct consequence of flare heating in the lower corona, and not due to the heating of breakout reconnection. This is reasonable as the breakout reconnection mainly removes the constraint of overlying loops to trigger the eruption without adding new layers to the flux rope (Antiochos et al. 1999). Lepri and Zurbuchen (2004) suggested that magnetic connectivity of the part of the ICME observed in situ to the flaring region is the key to the presence of high Fe charge states. Here, we propose a different scenario.

According to the CME model (Forbes & Acton 1996; Lin & Forbes 2000; Lin et al. 2004), the flux rope and the flare region can be related with each other through the reconnecting current sheet in the wake of a CME. The Fe ions with high/normal charge states can be generated in the high/normal temperature current sheet (e.g., Ciaravella et al. 2013), in addition to the flare region, and fill in the corresponding layers of the flux rope like ‘layers of an onion’ as mentioned (Ko et al. 2013). In this paper, the high/normal temperature in the current sheet is defined as it is beyond/below 2 MK. This is consistent with the early calculation of Arnaud & Raymond (1992), which showed that high Fe charge states ( $\geq 15+$ ) can have a considerable amount ( $> 30\%$ ) above 2 MK. We point out that the temperature of a flux rope will likely decrease with its expansion when propagating outward, therefore, the  $\langle Q \rangle_{\text{Fe}}$  within the flux rope when reaching the charge-state freezing distance may not be as high as that in the earlier reconnecting current sheet region (e.g., Rakowski et al. 2007; Ko et al. 2010). Based on these points, we present our understanding to the above observations in Figure 8 with some schematics.

The left panels show the eruption with a pre-existing flux rope as delineated with a yellow circle filled with blue, which means its  $\langle Q \rangle_{\text{Fe}}$  is lower than 12+. The large purple circle depicts the boundary of the MC. In panel (a1), the current sheet has a high temperature, this leads the  $\langle Q \rangle_{\text{Fe}}$  to be higher than 12+, as presented with red. As the ionic charge states are mostly frozen before they leave the corona (e.g., Rakowski et al. 2007; Ko et al. 2010), the measured MC will likely contain a low/high ionized center/shell. If the spacecraft passes through the MC along the upper green arrow, a bimodal distribution like Figure 3(f) will be detected. If the spacecraft passes through the MC shell portion along the lower arrow, a distribution shape as pointed with the arrow should be observed, similar to Figure 5(f). Panel (a2) describes the case that the current sheet temperature is high at first, but becomes normal subsequently during the flux rope formation. Then the MC will contain a high-ionization-state inner shell and a low-ionization-state outer shell. The obtained  $\langle Q \rangle_{\text{Fe}}$  shapes can be similar to Figures 3(f) or 4(f), depending on the spacecraft passage. It is also possible to get a distribution shape similar to Figure 6(f) if the spacecraft just passes through the MC edge, which is not plotted in panel (a2). Panel (a3) describes the case that the current sheet temperature is normal during the flux rope growth. Then no Fe ions with high charge states are available to fill in the flux rope, which results in the distribution shape like Figure



6(f), no matter where the spacecraft passes through the MC.

The right panels present the situation when the flux rope is formed during the eruption, so just a large purple circle is plotted at the MC boundary. Correspondingly, the top, middle, and bottom panels refer to cases of which current sheet temperature being high, first high then normal, and normal during the flux rope formation. It is easy to understand that three  $\langle Q \rangle_{\text{Fe}}$  distribution shapes can be obtained, except the bimodal distribution as shown in Figure 3(f). Therefore, our analysis suggests that the flux rope exists prior to the eruption if its MC  $\langle Q \rangle_{\text{Fe}}$  distribution presents the bimodal shape. In summary, the observed  $\langle Q \rangle_{\text{Fe}}$  distributions depend on how the spacecraft crosses the MC as well as physical properties of the flux rope and the current sheet near the Sun.

In order to support the above scenario, we checked the source regions of 11 CMEs in Group A with EIT on board the *Solar and Heliospheric Observatory* and  $\text{H}\alpha$  images from the Big Bear Solar Observatory. The results show that 7 (Events 1-6 and 8) of them are associated with filaments. This indicates a pre-existing flux rope (Rust & Kumar, 1994; Song et al. 2015a) and supports our scenario. We can not identify the source region for Event 7, and no filaments were observed in the source active regions for Events 9-11. It is not easy to confirm or deny the existence of other proxies of flux ropes prior to the eruptions, such as sigmoid structures (Titov & Démoulin, 1999) and/or hot channels (Zhang et al. 2012; Song et al. 2015b) as no soft X-ray and high temperature EUV observations available.

As mentioned, some disagreements on MC boundary locations often exist among different MC lists (e.g., Huttunen et al. 2005). To assess its influence to our statistical results, we checked another MC list ([http://wind.nasa.gov/index\\_WLICME\\_list.htm](http://wind.nasa.gov/index_WLICME_list.htm)) on the *WIND* website. As the *WIND* locates at L1 point since 2004, we mainly compared the 31 MCs appeared both in this list and our Table 1 between 2004 and 2009. The difference of their start/end time varies in a range of 0~5.5/0.5~16.3 h with the average value being 1.7/4.5 h, while the average of MC duration across the spacecraft is close to 20 h (e.g., Wu & Lepping, 2011, 2015). According to this MC list, only one event (20050612) of the 31 MCs should be reclassified and moved from Group C to B. This almost does not affect our statistics.

Considering the complex dynamical processes of magnetic reconnection and CME eruption, as well as the propagation of flux rope in interplanetary space, not all  $\langle Q \rangle_{\text{Fe}}$  distributions are regular inside MCs and can be classified into Groups A – D. Four such events (Group E) are found, indicating some complicated cases may exist. For example, when cold filament materials contained in MCs were detected in situ (Gloeckler et al. 1999; Lepri et al. 2010), the  $\langle Q \rangle_{\text{Fe}}$  will descend obviously and the charge-state distribution will change accordingly. The first event in Group E is probably such a case (Gloeckler et al. 1999), in which the  $\langle Q \rangle_{\text{Fe}}$  descends gradually from 16+ to 6+. The second event is odd with former/later part lower/higher than 12+ if the two discrete points beyond 12+ were neglected, and the rest two events show three peaks higher than 12+ inside the MCs. These events can not be explained with our simple and qualitative scenario.

We also note some high Fe charge states exist outside the MCs, e.g., the sheath region in Figure 5(e). They might be generated by processes such as the breakout reconnection or heating of a lower coronal shock. They may also correspond to the outermost part of the magnetic flux rope in the corona, but not regarded as parts of MCs possibly because of their irregular magnetic structure as measured in situ. For the high Fe charge states in ICMEs without an embedding MC, we speculate that they may also be produced by magnetic reconnection along the post-CME current sheet, yet the ejecta does not evolve into a regular MC structure.

## 5. SUMMARY

We made a comprehensive survey of  $\langle Q \rangle$ Fe distributions inside 96 MCs for solar cycle 23 using *ACE* data. The high Fe charge state is defined when the  $\langle Q \rangle$ Fe is larger than 12+, which means a considerable amount of Fe ions with high charge states (e.g.,  $\geq 16+$ ) appears inside the MCs. The statistical results show that the distribution of 92 MCs ( $\sim 96\%$ ) can be classified into four groups with different characteristics. Group A (11 MCs) is defined when the  $\langle Q \rangle$ Fe shows a bimodal distribution with its double peaks higher than 12+. Group B (4 MCs) presents a unimodal distribution with its peak higher than 12+. Groups C (29 MCs) and D (48 MCs) represent that the  $\langle Q \rangle$ Fe keeps always higher and lower than 12+ during *ACE* passage through the MC, respectively.

A qualitative scenario was proposed to explain the results, which can be used to infer the magnetic flux rope formation time and the current sheet temperature information during eruption. The high/normal Fe charge state indicates the current sheet temperature is high/normal during the eruption, and the bimodal distribution exists only if the flux rope has been formed prior to the eruption. Our study supports this scenario in a preliminary and statistical way. More detailed case studies are needed to further test this scenario.

We are grateful to the referee for his/her constructive comments and suggestions, which improved the paper greatly. We thank Susan T. Lepri, Lan Jian, Jun Lin, Yuming Wang, Pengfei Chen, Yong Liu, and Chenglong Shen for their valuable comments and discussion. We acknowledge the use of data from the *ACE* and *WIND* missions. This work is supported by the 973 program 2012CB825601, NNSFC grants 41274177, 41274175, and 41331068. J.Z. is supported by US NSF AGS-1249270 and NSF AGS-1156120. G. L. is supported by ATM-0847719 and AGS-1135432. The work of L.Z. is supported by NSF grant AGS-1432100 and AGS-1344835.

## REFERENCES

- Antiochos, S. K., DeVore, C. R., & Klimchuk, J. A. 1999, *ApJ*, 510, 485
- Arnaud, M., & Raymond, J. 1992, *ApJ*, 398, 394

- Bemporad, A., Poletto, G., Suess, S. T., et al. 2006, *ApJ*, 638, 1110
- Burlaga, L., Sittler, E., Mariani, F., & Schwenn, R. 1981, *J. Geophys. Res.*, 86, 6673
- Chen, J. 1996, *J. Geophys. Res.*, 101, 27499
- Cheng, X., Ding, M. D., Zhang, J., et al. 2014, *ApJ*, 789, 93
- Cheng, X., Zhang, J., Ding, M. D., Liu, Y., & Poomvises, W. 2013, *ApJ*, 763, 43
- Chi, Y., Shen, C., Wang, Y., Ye, P., & Wang, S. 2015, arXiv:1504.07849
- Ciaravella, A., Webb, D. F., Giordano, S., & Raymond, J. C. 2013, *ApJ*, 766, 65.
- Forbes, T. G., & Acton, L. W. 1996, *ApJ*, 459, 330
- Gloeckler, G., Cain, J., Ipavich, F. M., et al. 1998, *Space Sci. Rev.*, 86, 497
- Gloeckler, G., Fisk, L. A., Hefti, S., et al. 1999, *Geophys. Res. Lett.*, 26, 157
- Gopalswamy, N., 2006, *Space Sci. Rev.*, 124, 145
- Gosling, J. T., McComas, D. J., Phillips, J. L., & Bame, S. J. 1991, *J. Geophys. Res.*, 96, 7831
- Gruesbeck, J. R., Lepri, S. T., Zurbuchen, T. H., & Antiochos, S. K. 2011, *ApJ*, 730, 103
- Hu, Q., & Sonnerup, B. U. Ö. 2002, *Journal of Geophysical Research (Space Physics)*, 107, 1142
- Huttunen, K. E. J., Schwenn, R., Bothmer, V., & Koskinen, H. E. J. 2005, *Annales Geophysicae*, 23, 625
- Jian, L., Russell, C. T., Luhmann, J. G., & Skoug, R. M. 2006, *Sol. Phys.*, 239, 393
- Kilpua, E. K. J., Isavnin, A., Vourlidas, A., Koskinen, H. E. J., & Rodriguez, L. 2013, *Ann. Geophys.*, 31, 1251
- Ko, Y.-K., Raymond, J. C., Rakowski, C., & Rouillard, A. 2013, in *AIP Conf. Ser. 1539, SOLAR WIND 13: Proceedings of the Thirteenth International Solar Wind Conference*, ed. G. P. Zank et al. (Melville, NY: AIP), 207
- Ko, Y.-K., Raymond, J. C., Vrsnak, B., & Vujic, E. 2010, *ApJ*, 722, 625
- Lepping, R. P., Berdichevsky, D. B., Wu, C. C., et al. 2006, *AnGp*, 24, 215
- Lepping, R. P., Burlaga, L. F., & Jones, J. A. 1990, *J. Geophys. Res.*, 95, 11957
- Lepping, R. P., & Wu, C. C. 2010, *Ann. Geophys.*, 28, 1539
- Lepping, R. P., Wu, C.-C., & Berdichevsky, D. B. 2015, *Sol. Phys.*, 290, 553

- Lepping, R. P., Wu, C.-C., Berdichevsky, D. B., & Szabo, A. 2011, *Sol. Phys.*, 274, 345
- Lepri, S. T., & Zurbuchen, T. H. 2010, *ApJ*, 723, L22
- Lepri, S. T., & Zurbuchen, T. H. 2004, *Journal of Geophysical Research (Space Physics)*, 109, A01112
- Lepri, S. T., Zurbuchen, T. H., Fisk, L. A., et al. 2001, *J. Geophys. Res.*, 106, 29231
- Lin, J., & Forbes, T. G. 2000, *J. Geophys. Res.*, 105, 2375
- Lin, J., Raymond, J. C., & van Ballegooijen, A. A. 2004, *ApJ*, 602, 422
- Lynch, B. J., Reinard, A. A., Mulligan, T., et al. 2011, *ApJ*, 740, 112
- McComas, D. J., Bame, S. J., Barker, P., et al. 1998, *Space Sci. Rev.*, 86, 563
- Mikić, Z., & Linker, J. A. 1994, *ApJ*, 430, 898
- Ouyang, Y., Yang, K., & Chen, P. F. 2015, *ApJ*, 815, 72
- Patsourakos, S., Vourlidas, A., & Stenborg, G. 2013, *ApJ*, 764, 125
- Rakowski, C. E., Laming, J. M., & Lepri, S. T. 2007, *ApJ*, 667, 602
- Rust, D. M., & Kumar, A. 1994, *SoPh*, 155, 69
- Shearer, P., von Steiger, R., Raines, J. M. et al. 2014, *ApJ*, 789, 60
- Smith, C. W., L’Heureux, J., Ness, N. F., et al. 1998, *Space Sci. Rev.*, 86, 613
- Song, H. Q., Chen, Y., Zhang, J., et al. 2015a, *ApJ*, 804, L38
- Song, H. Q., Chen, Y., Zhang, J., et al. 2015b, *ApJ*, 808, L15
- Song, H. Q., Zhang, J., Chen, Y., & Cheng, X. 2014a, *ApJ*, 792, L40
- Song, H. Q., Zhang, J., Chen, Y., et al. 2015c, *ApJ*, 803, 96
- Song, H. Q., Zhang, J., Cheng, X., et al. 2014b, *ApJ*, 784, 48
- Titov, V. S., & Démoulin, P. 1999, *A&A*, 351, 707
- von Steiger, R., Schwadron, N. A., Fisk, L. A. et al. 2000, *J. Geophys. Res.*, 105, 27217
- Wang, Y., Zhou, Z., Shen, C., Liu, R., & Wang, S. 2015, *Journal of Geophysical Research (Space Physics)*, 120, 1543
- Wu, C.-C., & Lepping, R. P. 2011, *Sol. Phys.*, 269, 141

Wu, C.-C., & Lepping, R. P. 2015, *Sol. Phys.*, 290, 1243

Zhang, J., Dere, K. P., Howard, R. A., & Bothmer, V. 2003, *ApJ*, 582, 520

Zhang, J., Richardson, I. G., Webb, D. F., et al. 2007, *Journal of Geophysical Research (Space Physics)*, 112, A10102

Zhang, J., Cheng, X., & Ding, M.-D. 2012, *Nature Communications*, 3, 747

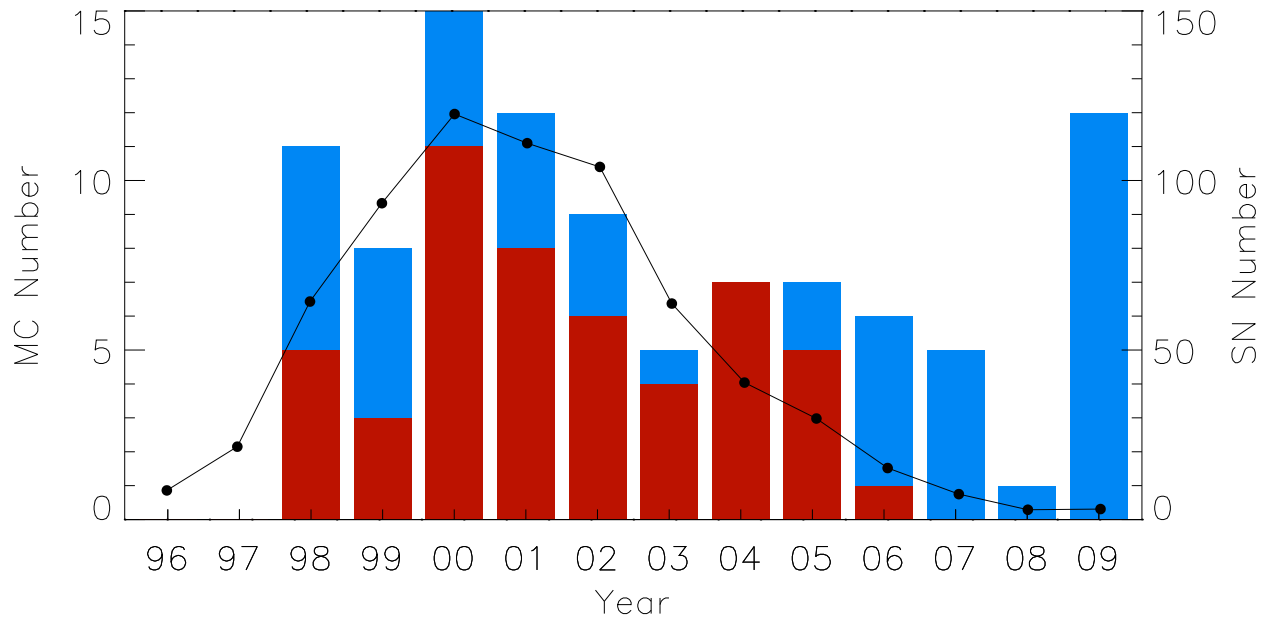


Fig. 1.— Yearly number of MCs in the study. The blue/red portions of the bars correspond to the MCs without/with high Fe charge state. The line connected by the filled circles shows the yearly sunspot number.

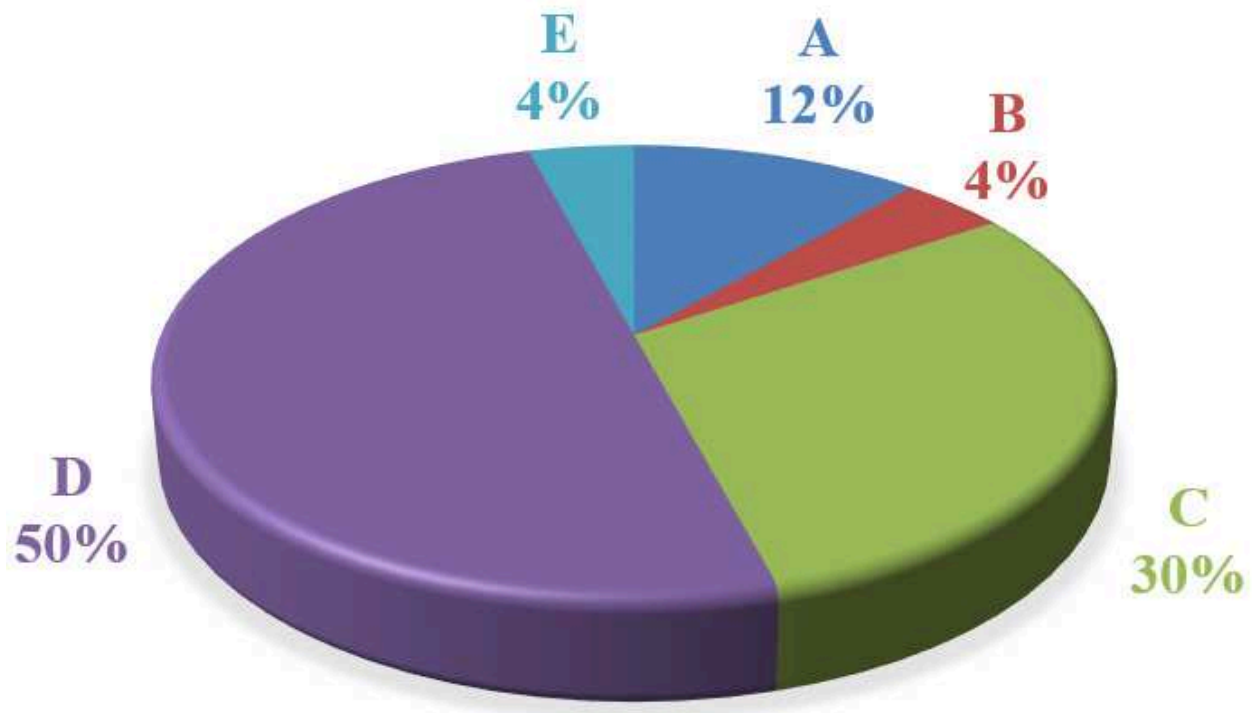


Fig. 2.— Pie diagram that shows the percentages of different groups for the 96 MCs with complete Fe charge-state data.

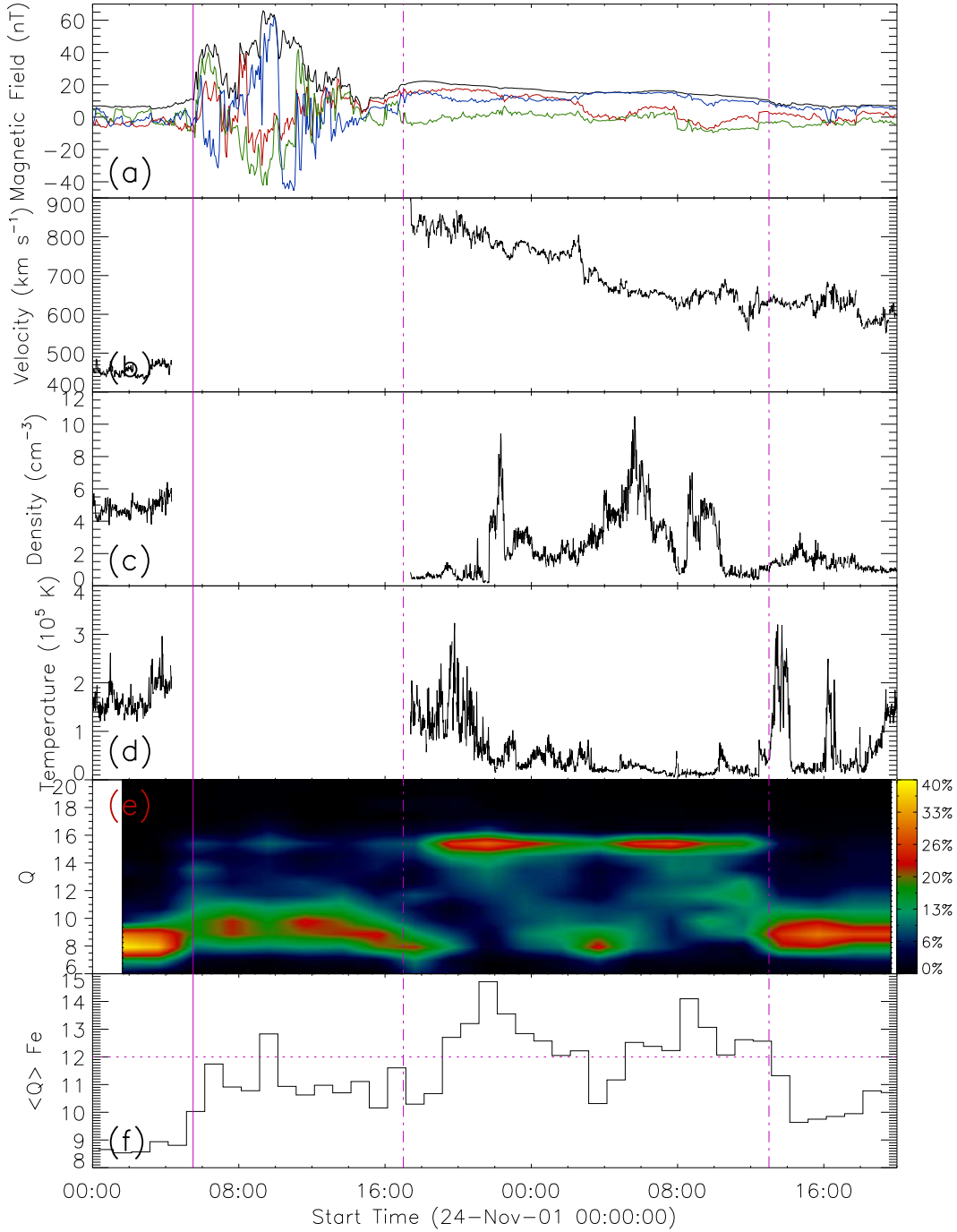


Fig. 3.— Solar wind parameters and charge-state distribution measured with *ACE* for 20011124 event in Group A. (a) the total magnetic field strength (black line) and the X (red), Y (green), and Z (blue) components in the GSE coordinate, (b)-(d) the bulk speed, density, and temperature of solar wind, (e) 3D Fe charge-state-distribution map, and (f) the  $\langle Q \rangle_{\text{Fe}}$ . The horizontal purple dotted line marks the level of 12+. The locations of the ICME shock and MC boundaries are depicted with purple vertical solid line and dot-dashed lines, respectively.



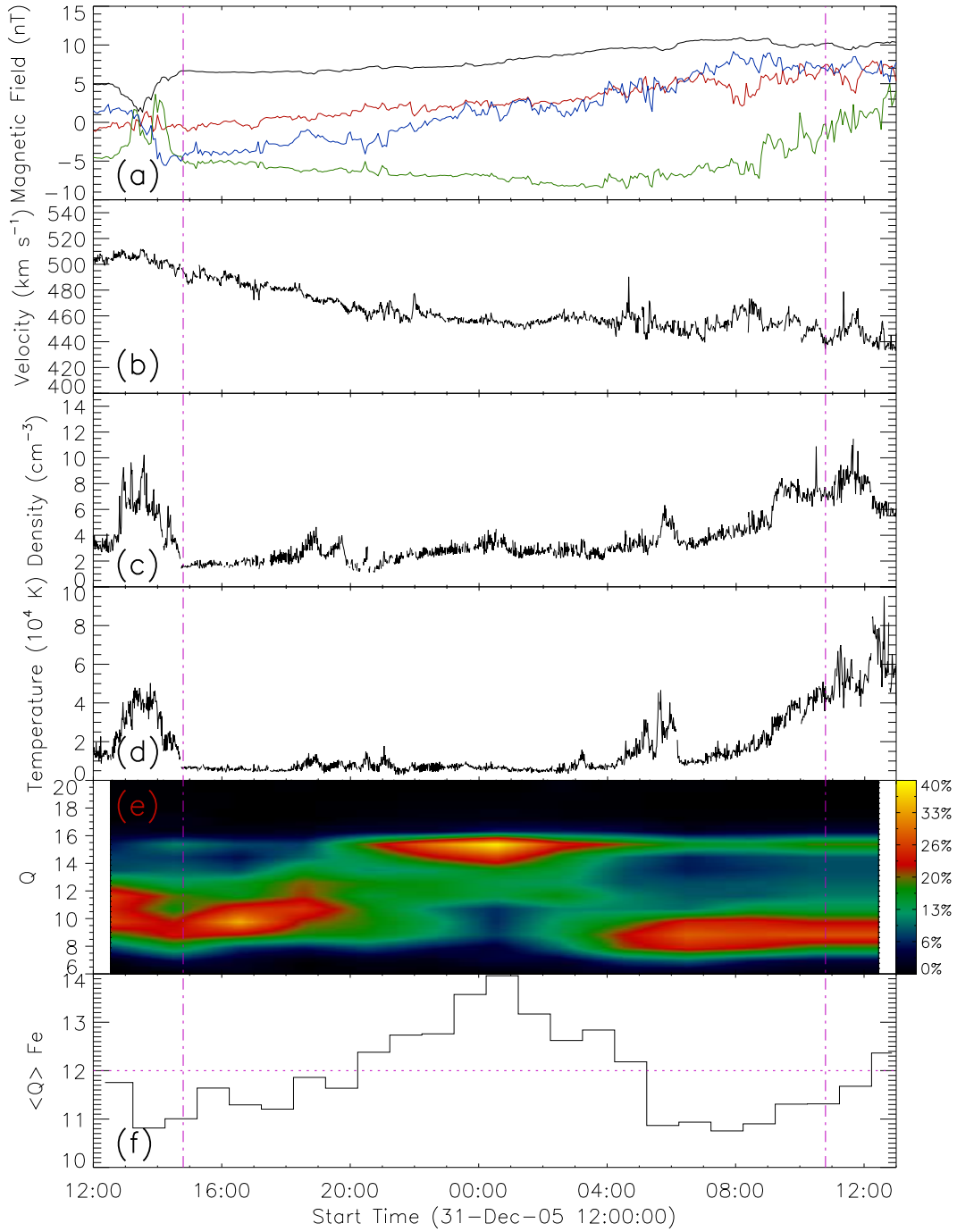


Fig. 4.— Same as Figure 3 but for 20051231 event in Group B.

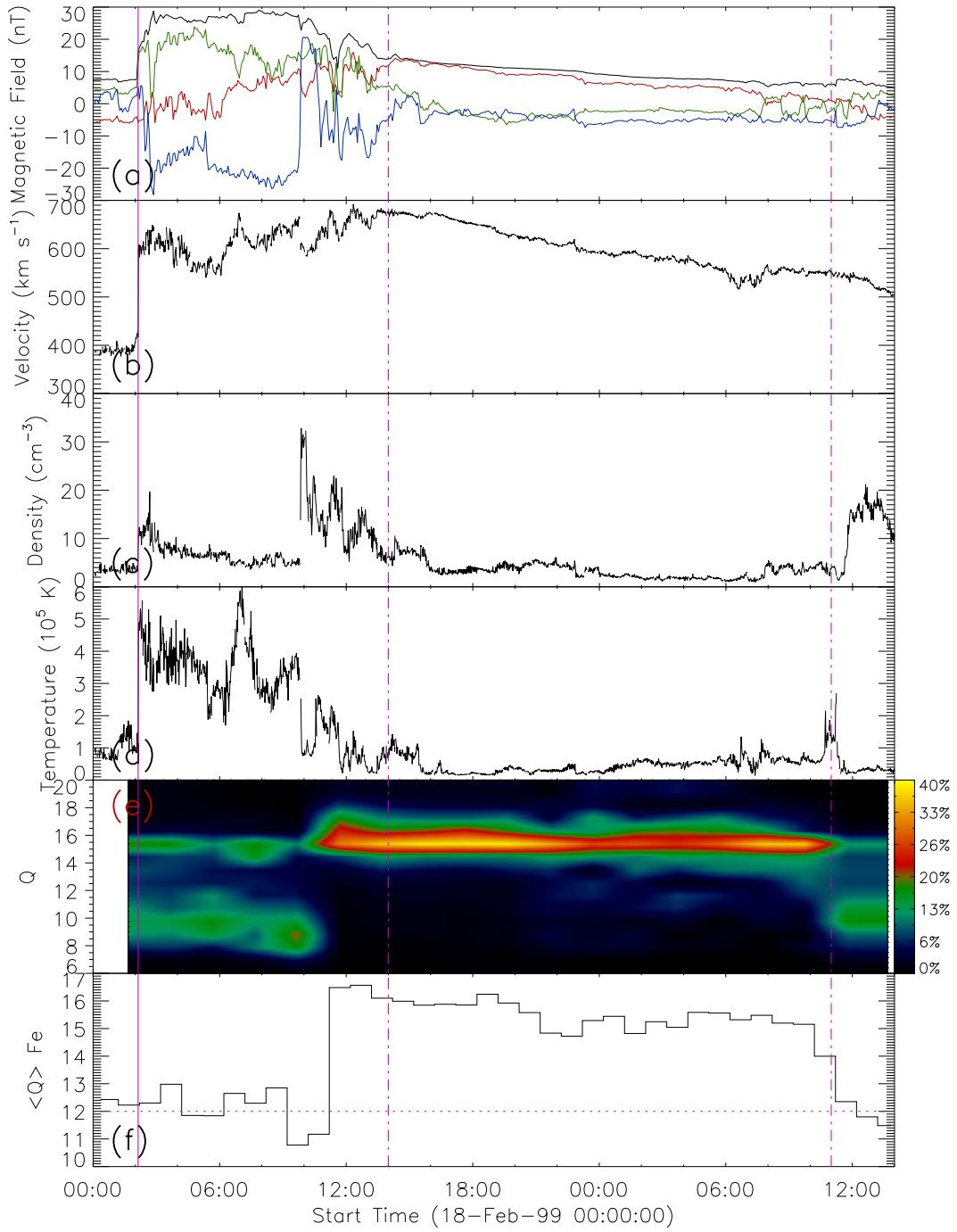


Fig. 5.— Same as Figure 3 but for 19990218 event in Group C.

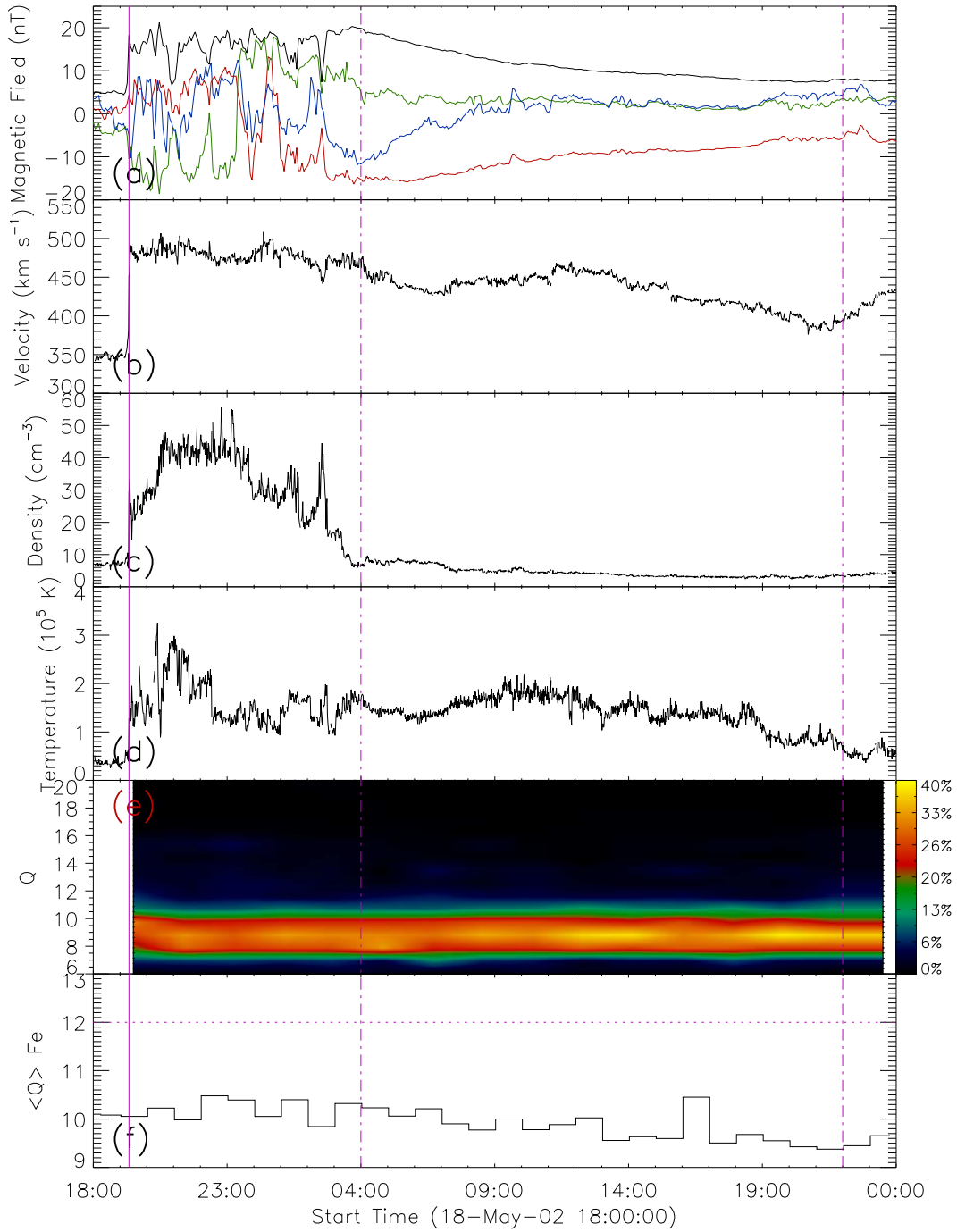


Fig. 6.— Same as Figure 3 but for 20020519 event in Group D.

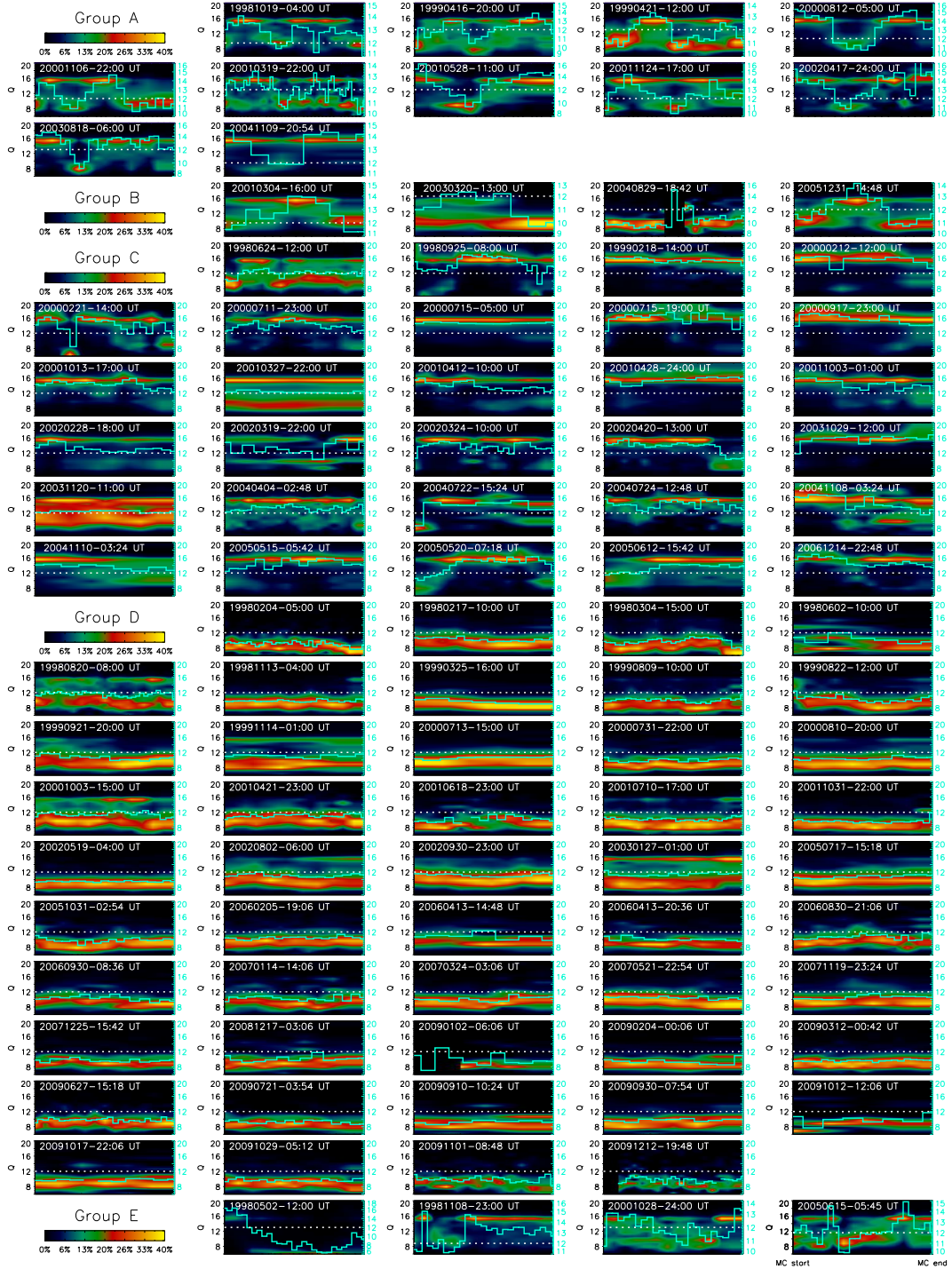


Fig. 7.— The Fe charge state distributions and  $\langle Q \rangle_{\text{Fe}}$  variations (cyan) within 96 MCs. The horizontal white dotted lines mark the level of 12+ for  $\langle Q \rangle_{\text{Fe}}$ . Groups A, B, C and E are all associated with lots of high Fe charge states, while Group D is mainly associated with normal Fe charge states with  $\langle Q \rangle_{\text{Fe}}$  below 12+. The left/right boundary corresponds to each MC start/end time. See text for details.

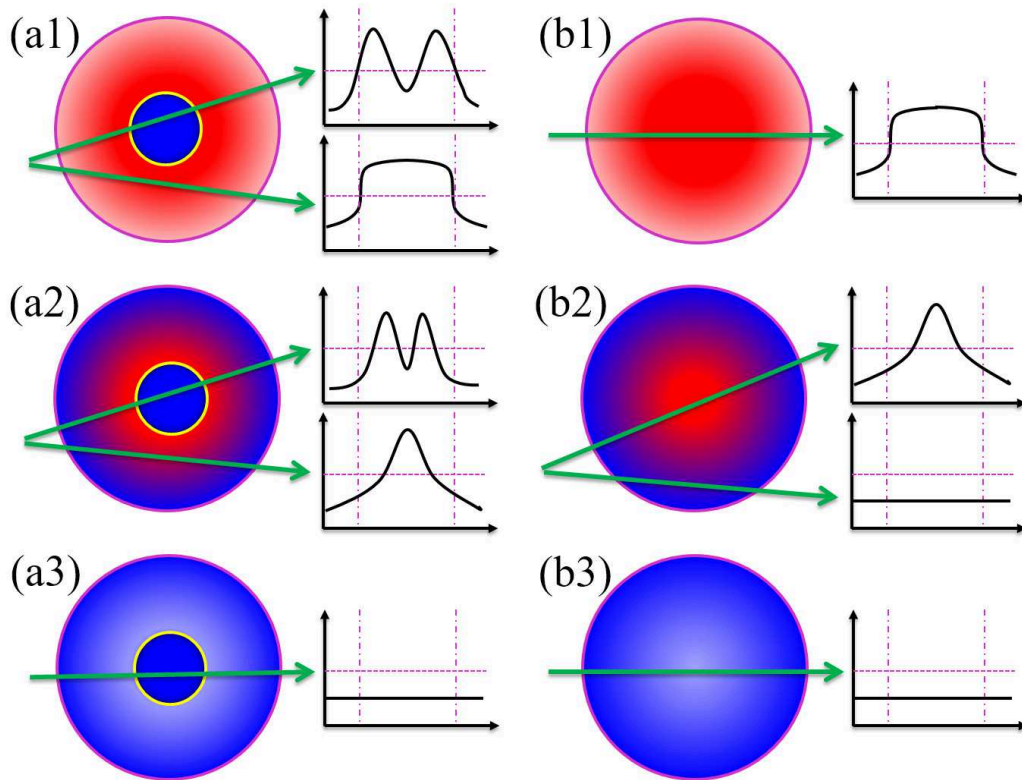


Fig. 8.— Schematic drawings of the explanation for the  $\langle Q \rangle \text{Fe}$  distributions inside MCs. Red/blue denotes the  $\langle Q \rangle \text{Fe}$  higher/lower than 12+. The horizontal purple dotted lines in the coordinates mark the  $\langle Q \rangle \text{Fe}$  level of 12+, and the purple vertical dot-dashed lines demarcate the MC boundaries. See text for details.